Available online at www.sciencedirect.com
ScienceDirect
Acta Materialia 56 (2008) 602–608
Acta MATERIALIA
www.elsevier.com/locate/actamat

A search for evidence of strain gradient hardening in Au submicron pillars under uniaxial compression using synchrotron X-ray microdiffraction

A.S. Budiman [a,*], S.M. Han [a], J.R. Greer [b], N. Tamura [c], J.R. Patel [a,c], W.D. Nix [a]

[a] *Department of Materials Science and Engineering, Stanford University, Stanford, CA 94305, USA*
[b] *Department of Materials Science, California Institute of Technology, Pasadena, CA 91125, USA*
[c] *Advanced Light Source (ALS), Lawrence Berkeley National Laboratory (LBNL), CA 94720, USA*

Received 23 May 2007; received in revised form 12 October 2007; accepted 13 October 2007
Available online 19 December 2007

Abstract

When crystalline materials are mechanically deformed in small volumes, higher stresses are needed for plastic flow. This has been called the "smaller is stronger" phenomenon and has been widely observed. Various size-dependent strengthening mechanisms have been proposed to account for such effects, often involving strain gradients. Here we report on a search for strain gradients as a possible source of strength for single-crystal submicron pillars of gold subjected to uniform compression, using a submicron white-beam (Laue) X-ray diffraction technique. We have found, both before and after uniaxial compression, no evidence of either significant lattice curvature or subgrain structure. This is true even after 35% strain and a high flow stress of 300 MPa were achieved during deformation. These observations suggest that plasticity here is not controlled by strain gradients or substructure hardening, but rather by dislocation source starvation, wherein smaller volumes are stronger because fewer sources of dislocations are available.

Keywords: Materials with reduced dimensions; Size effects; Dislocation; Synchrotron radiation; X-ray diffraction (XRD)

1. Introduction

Investigations of the role of length scales in the mechanical behavior of materials have great importance to the field of materials science, especially in today's nano-age where submicron and nanoscale devices are built near the size of their microstructural features. The creation of such small components requires a thorough understanding of the mechanical properties of materials at these small length scales. In the macroscale (bulk), the mechanical properties of materials are commonly described by single-valued parameters (yield stress, hardness, etc.), which are largely independent of the size of the specimen. However, as specimens are reduced in size to the scale of the microstructure, their mechanical properties deviate from those of bulk materials. For example, in thin films – where only one dimension, the thickness, reaches the micron scale and below – the flow stress is found to be higher than its bulk value, and becomes even higher as the film gets thinner. This size effect is usually attributed to the confinement of dislocations by the substrate [1–3].

In nanoindentation experiments, where the length scale of the deformation reaches the microstructural length scale of the material, the governing relations between stress and strain deviate from the classical laws that apply to bulk materials. At small indentation depths the hardness of crystalline materials is usually higher than that of large indentations. This indentation size effect (ISE) has been explained using the concept of geometrically necessary dislocations (GNDs) and strain gradients [4–17]. According to this picture, the hardness increases with decreasing depth

* Corresponding author.
E-mail address: suriadi@stanford.edu (A.S. Budiman).

1359-6454/$30.00
doi:10.1016/j.actamat.2007.10.031

of indentation because the total length of geometrically necessary dislocations forced into the solid by the self-similar indenter scales with the square of the indentation depth, while the volume in which these dislocations are found scales with the cube of the indentation depth. This leads to a geometrically necessary dislocation density that depends inversely on the depth of indentation. The higher dislocation densities expected at smaller depths leads naturally to higher strengths through the Taylor relation, and this leads to the ISE [18].

Recently Uchic et al. [19] and others [20,21] have shown that micropillars of various metals with diameters in the micron range, subjected to uniaxial compression, are much stronger than bulk materials. For example, micropillars of gold ranging in diameter from 200 nm to several microns have been found to have compressive flow strengths as high as 800 MPa, a value ~50 times higher than the strength of bulk gold [20,21]. However, in spite of much progress on size effects on strength there is still no unified theory for plastic deformation at the submicron scale. The accounts of strain gradient plasticity, as discussed above, appear to break down for the case of micropillar compression because the geometry of the micropillar compression is not expected to include externally imposed plastic strain gradients that might lead to extra hardening for small samples.

While significant macroscopic strain gradients are not expected to develop during the uniform compression of micron-sized pillars, we can not preclude microscopic strain gradients from forming. Nevertheless, even the presence or the absence of macroscopic strain gradients has not been directly and experimentally observed, especially in the case of metallic pillars. Since strain gradients and GNDs are directly related to the local lattice curvature, the technique of scanning X-ray microdiffraction (μ-SXRD) using a focused polychromatic/white synchrotron X-ray beam can be used to determine the density of GNDs. This has proven to be useful in the study of the early stages of electromigration failure in interconnect lines, wherein lattice bending and GNDs are created by electromigration processes [22,23]. This capability is related to the continuous range of wavelengths in a white X-ray beam, allowing Bragg's Law to be satisfied even when the lattice is locally rotated or bent, resulting in the observation of streaked Laue spots.

Using this approach, we can monitor the change in the Laue diffraction peaks before and after uniaxial compression of a submicron single-crystal Au pillar. A quantitative analysis of the Laue peak widths then allows us to estimate the density of GNDs in the pillar. The absolute number of geometrically necessary dislocations in the crystal can then be determined using the dimensions of the pillar. A comparison of the numbers of geometrically necessary dislocations before and after the uniaxial compression provides information about the change in microstructure associated with plastic deformation.

The technique of synchrotron-based white beam X-ray diffraction is one of the few methods for detecting and measuring the densities of GNDs in crystalline materials after deformation. Other viable techniques include transmission electron microscopy (TEM) and resonant ultrasound spectroscopy (RUS) [24].

The synchrotron technique of scanning white beam X-ray microdiffraction has been described thoroughly elsewhere [25]. The power of this technique to study local plasticity and mechanical behavior of materials at small scales stems from the high brilliance of the synchrotron source, as well as the recent advances in X-ray focusing optics (allowing sample mapping at the submicron level).

2. Experimental

The sample consists of a four-crystal film of Au oriented ⟨1 1 1⟩ out-of-plane (Fig. 1), and deposited onto a ⟨0 0 1⟩ Cr single-crystal substrate, in the form of a 2 mm thick, 10 mm diameter disk. The native oxide on the surface of the Cr substrate was first removed by ion cleaning in a high vacuum, using the appearance of a reflection high energy electron diffraction (RHEED) pattern of single-crystal Cr to indicate the removal of the surface oxide. A thin layer of Au was then epitaxially deposited onto the bare Cr surface by vapor deposition in the same high vacuum chamber, before moving the sample to a sputtering system to continue growth to a thickness of 1.9 μm. While a ⟨0 0 1⟩ orientation was expected for the Au film on the basis of interface energy considerations, the low energy of the (1 1 1) surface must have caused the ⟨1 1 1⟩ orientation to be selected. For this orientation, a nearly perfect lattice match is achieved along a ⟨1 1 0⟩ direction in the (1 1 1) surface of Au and a ⟨1 0 0⟩ direction in the (0 0 1) surface of Cr.

The pillars were fabricated utilizing the method of focused ion beam (FIB) machining, following the approach developed by Greer and Nix [21]. Circular craters 30 μm in diameter were first carved out of the Au film, leaving behind only the submicron pillars at the centers of the craters (Fig. 2a and b). Using scanning electron microscopy, we determined that the Au pillar (Fig. 2c) was a bicrystal of Au with top and bottom crystals having different in-plane orientations. The top crystal was about 1.1 μm in height and became the focus of our experiment. It has diameter of 0.58 μm, leading to a height-to-diameter ratio of close to 2:1 for that crystal. The lower crystal was about 0.8 μm in height (and also 0.58 μm in diameter) and misoriented with respect to the upper crystal by about 30° (in-plane orientations). We could not rule out that the lower crystal might have deformed too in response to pillar compression; also the lower crystal might present a barrier to dislocation motion in the upper crystal. However, this barrier would not be stronger than having the Cr substrate on the bottom of the upper crystal.

The uniaxial compression testing of these submicron pillars was conducted using an MTS Nanoindenter XP with a flat punch diamond tip, following the methodology described by Han [26]. The nanoindenter, which is a load-controlled instrument, was programmed to perform

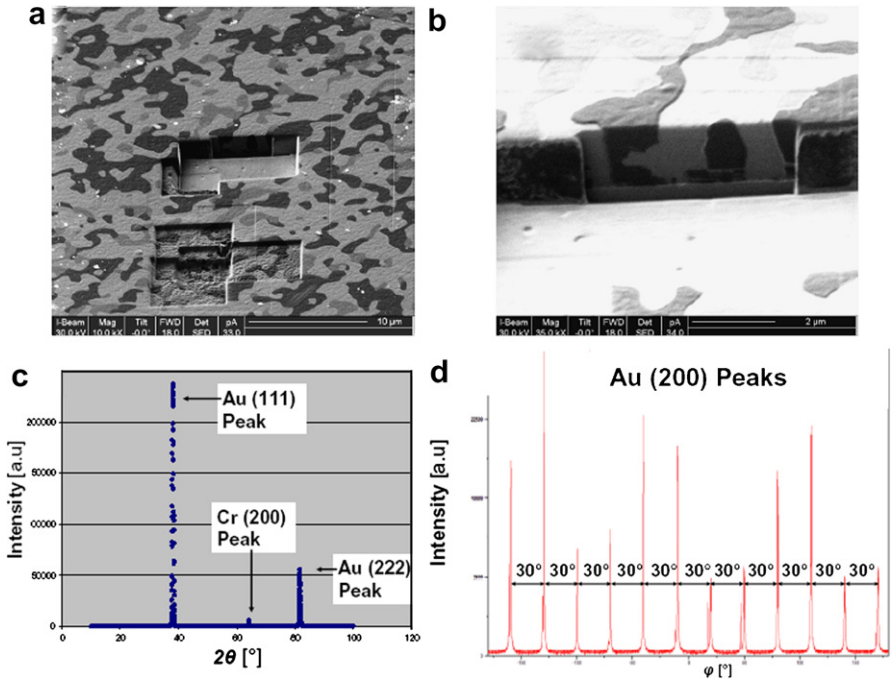

Fig. 1. The Au (1 1 1) film on Cr (2 0 0) substrate: (a) four variants of Au ⟨1 1 1⟩ out-of-plane crystals were observed in the planar view, as well as (b) through thickness of film (using ion beam contrast imaging inside a scanning electron microscope at a 52° tilted angle); (c) symmetric X-ray diffraction gave the Au (1 1 1) peaks of the film and the Cr (2 0 0) peak of the single-crystal Cr substrate; however (d) non-symmetric X-ray diffraction (by tilting the sample 54.74° to get Au (2 0 0) peaks, and then scanning ϕ for 360°) gave four sets of three Au (2 0 0) peaks each separated by 120° angle, indicating the four-crystal Au ⟨1 1 1⟩ film.

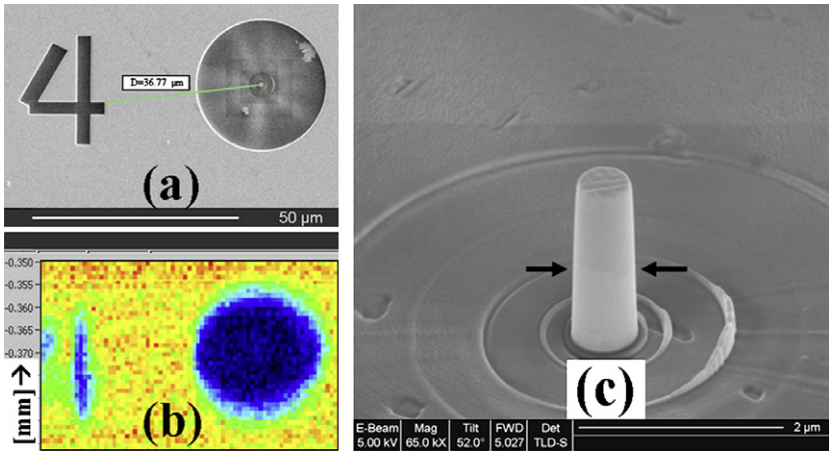

Fig. 2. The submicron Au pillar specimen: (a) the crater in the middle of which stands the pillar, with the identifying mark (number "4") on the left (SEM image), and (b) synchrotron white-beam X-ray microfluorescence (XRF) scan; (c) a ⟨1 1 1⟩-oriented gold pillar machined in the FIB (pillar diameter = 580 nm, pillar height = 1.9 μm (total) and ~1.1 μm (the upper crystal); a slight color contrast signifying differently oriented crystals between the upper and bottom crystals is visible upon careful inspection, as indicated by the arrows pointing to the interface).

a nominally displacement-controlled test. In this method, the displacement rate is calculated continuously during the compression test, based on the measured displacement and time. When the measured displacement rate is below a specified value, the load is adjusted to maintain that particular displacement rate. This method is designed to simulate a constant displacement rate. Load–displacement data were collected in the continuous stiffness measurement (CSM) mode of the instrument. The data obtained during compression were then converted to uniaxial stresses and strains using the assumption that the plastic volume is conserved throughout this mostly homogeneous deformation.

The white beam X-ray microdiffraction experiment (Fig. 3) was performed on beamline 7.3.3 at the Advanced Light Source, Berkeley, CA. The sample was mounted on a precision XY Huber stage and the pillar of interest was raster scanned at room temperature under the X-ray beam before and after the uniaxial compression (ex situ); this provided

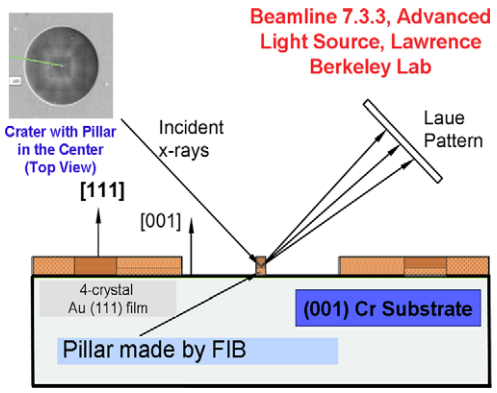

Fig. 3. A schematic illustration of the synchrotron white-beam X-ray microdiffraction experiments (conducted at the ALS beamline 7.3.3, Lawrence Berkeley National Lab) on the Au submicron pillar on Cr substrate.

X-ray microfluorescence (μXRF) and X-ray microdiffraction (μXRD) scans for the area near the pillar. The μXRD patterns were collected using a MAR133 X-ray CCD detector and analyzed using the XMAS software package.

The μXRF scan was conducted first for precise positioning of the Au pillar prior to the μXRD scan. The μXRF scan was made using 1 μm step sizes to cover a large area of typically 70×70 μm (to include not only the 30 μm diameter crater, but also the identifying mark: number "4" in Fig. 1). The circular crater was used, first, to clearly locate the position of the pillar (as the pillar was fabricated at the center of the crater), and, secondly, to partially separate the diffraction signal of the pillar from that of the surrounding gold film, such that only those diffracted beams from the pillar (and not those of the surrounding film) can be studied.

Once the Au pillar was located and identified, a μXRD scan was conducted to obtain diffraction data primarily from the Au crystal/pillar. The typical scan for this purpose was made with 1 μm step sizes, 50 steps across the diameter of the crater (50 μm scan length) and 10 steps along its orthogonal direction (10 μm scan length), making it a wide band of 50×10 μm. This scan area was designed to include not only the pillar, but also the boundaries of the crater with the surrounding Au film as positional references. This μXRD scan involved the collection of 500 CCD frames. A complete set of CCD frames took about 4–5 h to collect. The exposure time was 5 s, in addition to about 10 s of electronic readout time for each frame.

With μXRD, we monitored the change in the Laue diffraction images before and after uniaxial compression of a single-crystal submicron Au pillar. A quantitative analysis of the Laue peak widths allows us to estimate the density of GNDs in the submicron single-crystal pillars. As the exact geometries of the pillars are known, the absolute number of dislocations in the single-crystal can be derived. A comparison of the numbers of dislocations before and after the uniaxial compression would unveil the change in the structure involved in the deformation.

3. Results and discussion

Fig. 4 shows the mapping of the $(\bar{3}11)$ Laue diffraction spot from the top crystal of the pillar with the incident X-ray beam located at various positions in the vicinity of the pillar and crater, before any compressive deformation. Here, and hereafter, all of our attention will be focused on the upper crystal in the Au pillar structure.

Each of the individual images of the Laue diffraction spots in Fig. 4 represents a (diffracted) intensity contour in a two-dimensional (2-D) χ–2θ coordinate system (i.e. the 2-D coordinate in the diffractometer coordinate system). As we set the threshold of the lower-bound intensity display to be the same for all images, the difference in peak size/width in the mapping indicates a difference in the absolute diffracted intensity of the Au crystal volume at a particular position in the map. Thus, the size of the red "dots" is directly related to the diffracted volume of Au crystal. The bigger red "dots" on the left-hand and right-hand sides of this map clearly represent the surrounding Au films, while the smaller red dots in the middle area represent the crater (close to zero diffracting volume). Obviously, as there is no Au crystal away from the center of the crater, there ought to be absolutely zero diffraction intensity in this area. However, because of the Lorentzian shape of the incoming focused X-ray beam, the tails of the beam extend beyond (up to tens of microns) the nominal full width at half maximum (FWHM) (~1 μm) of the beam. Therefore, even though the beam is focused on a particular location in the crater, there is still a very small fraction of diffraction intensity coming from the surrounding film picked up by the tails of the X-ray beam.

The diffraction map in Fig. 4 also indicates unambiguously the exact location of the pillar itself (marked by the solid line box in Fig. 4). After subtracting out the diffraction intensity by the tails of the X-ray beam, a significant diffraction intensity was still left on the location at the centre of the solid line box (i.e. the pillar). This is so as there is indeed slightly more volume of Au crystal to diffract at the

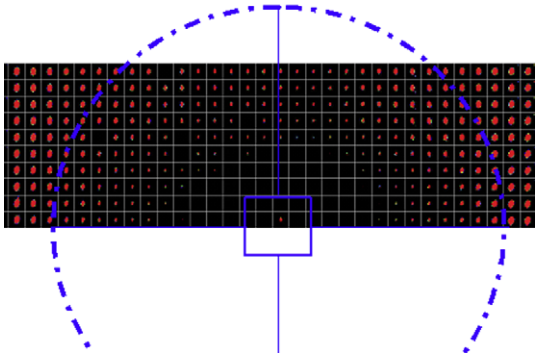

Fig. 4. A mapping of the $(\bar{3}11)$ Laue spot of the upper crystal of the pillar in the areas surrounding the pillar and the crater; step size = 1 μm. The dashed and dotted circle represents the 30 μm crater, and, as expected, exactly in the middle of it stands the pillar as marked by the rectangular solid line box.

location of the pillar, but this intensity is not as high as in the surrounding film areas (thus the relative size of the peak). The location associated with the slightly bigger Laue diffraction spot also coincides with the center of the crater as identified by dashed and dotted circle in the map of Fig. 4.

Fig. 5a shows the stress–strain curves of the 0.58 μm Au pillar obtained during the compression testing. Uniaxial loading in the ⟨1 1 1⟩ direction of the Au crystal/pillar, corresponding to a high symmetry orientation, would result in the activation of multiple slip systems, with the pillar deforming uniformly around its diameter as it is compressed. The flow stress reaches value as high as 280 MPa. This is close to 10 times the yield stress of gold in bulk, and falls consistently in the flow stress vs. pillar diameter chart described by Greer and Nix [21]. In this ⟨1 1 1⟩ loading orientation, and despite the presence of the end constraints, the pillar remains centrally loaded and preserves its cylindrical shape throughout the deformation process as shown in Fig. 5b. While upon further inspection we could not observe slip steps on the surface of the deformed pillar, we do however observe a visible slip marking (not shown very clearly in this particular SEM image in Fig. 5b) that appears to be consistent with the trace of a {1 1 1} plane of the pillar crystal. The angle made by the plane causing the trace was within a few degrees of the expected trace of a {1 1 1} plane, after correcting for subsequent plastic deformation of the pillar. The final diameter of the pillar after the uniaxial compression is 0.67 μm, which represents a total strain of close to 35%.

A diffraction scan was again taken covering the deformed pillar and the surrounding area (including the crater border with the surrounding Au film) similarly to the diffraction map in Fig. 4. Following the methodology described above, we again identify the location of the deformed pillar, and subsequently we select a particular Laue diffraction spot (in the case shown here, the $(\bar{3}1\,1)$ diffraction spot) associated with the location of the deformed pillar for further quantitative analysis and comparison. We subtracted the background intensity and checked that there is no Au crystal rotation involved (which would have manifested in the shift of the position of the Au Laue peak with respect to the Laue diffraction pattern of the chromium substrate reference), in order to be able to directly compare the $(\bar{3}1\,1)$ Laue spots before and after deformation and infer what happened to the pillar crystal during the deformation process. Fig. 6 shows the data of the pillar crystal (SEM images, Laue diffraction spots and intensity profiles) for both undeformed and deformed states side by side.

Fig. 6b shows that both $(\bar{3}1\,1)$ Laue spots have the same shape and that they are both rounded – not broadened toward a certain direction (streaked). This rounded shape is typical of an undeformed crystal, whereas broadening of a Laue diffraction spot in a certain direction (streaking) would have been associated with the presence of strain gradients in the deformation volume. A more detailed treatment of the streak length and its correlation with the curved, or in general, plastically deformed crystal has been described elsewhere [22,23]. In addition, streaked Laue diffraction spots have also been observed recently in as-fabricated silicon micropillars [27].

In Fig. 6c we take the intensity traces along a particular χ to study the Laue diffraction peak profile more quantitatively (here the χ angle is simply the angle orthogonal to the 2θ angle). The profiles were fitted with Lorentzian curves. The measured FWHMs of both profiles show that there is an increase of 0.01° in the angular width. However, this

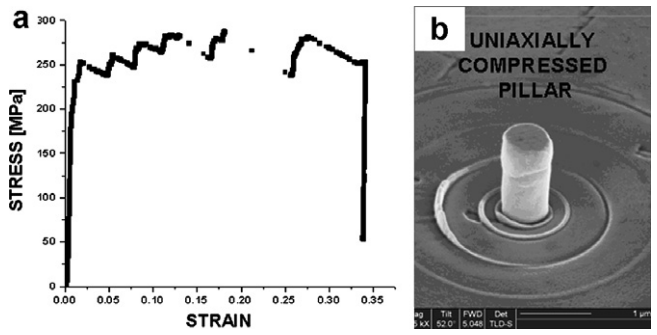

Fig. 5. Stress–strain behavior of ⟨1 1 1⟩-oriented Au single-crystal submicron pillar: (a) flow stress increases significantly beyond its typical bulk values; (b) SEM image of a uniaxially compressed pillar after deformation.

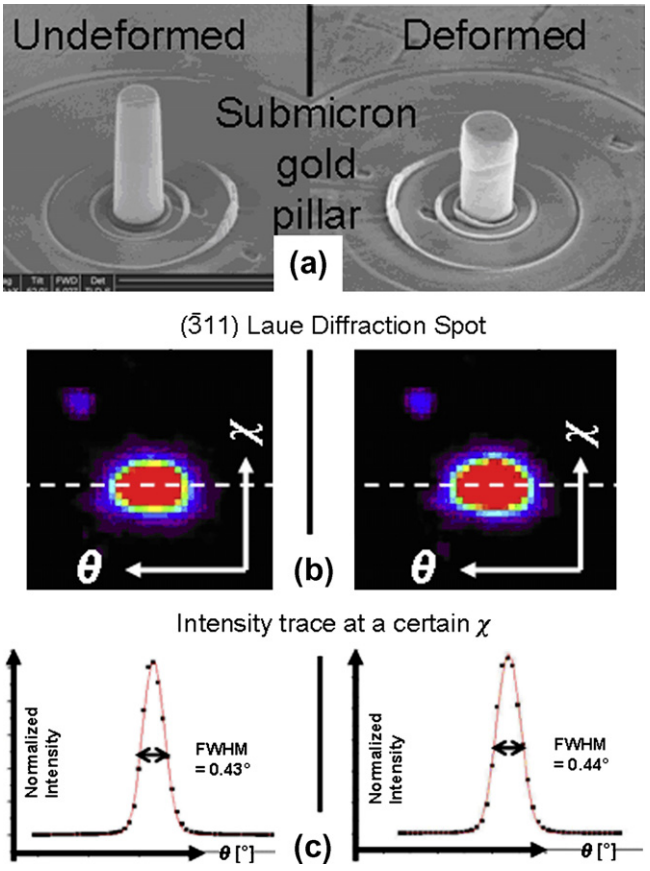

Fig. 6. Side-by-side comparison between undeformed and deformed states of the pillar crystal; (a) SEM images of the Au pillar, (b) $(\bar{3}1\,1)$ Laue diffraction spots and (c) quantitative analysis.

difference is still within the experimental error bar of the instrumentation [25,28], rendering the two measurements statistically identical. The angular resolution of this technique was calculated using a few assumptions on the experimental sample setup with respect to the CCD camera and on the capability of the indexing code [28], which are applicable to our micropillar compression experiments. The technique is sensitive to local lattice rotation, and thus this angular detection limit is applicable to GNDs.

In terms of the capability of this technique to detect GNDs, it is also limited by the instrumental broadening inherent in the observed Laue diffractions spots. One practical way to estimate the extent of instrumental broadening in our experiments is to take FWHM measurements of Laue diffraction spots coming from a silicon substrate/wafer, as such single-crystals are very close to being defect-free and 100% pure. Based on measurements on such silicon wafer substrates, for similar experimental settings, the instrumental broadening contribution to the observed FWHM of Laue diffraction spots is 0.06°. This places a limit on our technique corresponding to the number of GNDs associated with a peak broadening of 0.06°.

This limitation indicates that relative lattice rotations smaller than $\Delta\theta = 0.06°$, or $\Delta\theta = 10^{-3}$ radians, which might be produced by compressive deformation, could not be detected. Converting that measurement to the possible number of dislocations that could be left in the crystal after deformation depends on how the dislocations are distributed. To make these calculations we consider the model shown in Fig. 7 where different domains of size Δs are each assumed to be occupied by like-signed edge dislocations, leading to a local lattice curvature of magnitude $|\kappa|$. Thus within each domain there are only geometrically necessary dislocations. Taken over the whole crystal the dislocations can be regarded as statistically stored dislocations. We know from the Cahn–Nye relationship [29,30] that the local geometrically necessary dislocation density is $\rho = |\kappa|/b$, where b is the magnitude of the Burgers vector. But the local curvature is $|\kappa| = \mathrm{d}\theta/\mathrm{d}s \approx \Delta\theta/\Delta s$, so that $\rho = \Delta\theta/b\Delta s$. With this model the total number of dislocations in the entire crystal would be $n = \rho WH = WH\Delta\theta/b\Delta s$. Taking the dimensions of the upper crystal to be $W = 600$ nm and $H = 1100$ nm, and the Burgers vector to be $b = 0.3$ nm and using the X-ray broadening resolution of $\Delta\theta = 10^{-3}$, we find $n = 2.2 \times 10^3/\Delta s$. When the domain size is the same as the width of the crystal, $\Delta s = 600$ nm, this leads to 3–4 dislocations left in the crystal after deformation. The expected number of dislocations that could be left in the crystal after deformation naturally increases with decreasing domain size. In the limit, a very high density of statistically stored dislocations cannot be ruled out by these experiments, though escape of these dislocations from the nearby free surfaces makes this unlikely.

Thus the fact that the Laue diffraction spot in the deformed pillar is not streaked suggests that there might not be significant macroscopic strain gradients created during the uniaxial compression of the pillar (only 3–4 GNDs left in the crystal after deformation when the domain size is taken as the same as the width of the crystal, $\Delta s = 600$ nm). However, within the resolution and limitation of our technique, we could not preclude the existence of microscopic strain gradients within the inspected volume, as illustrated in Fig. 7. In addition, as we find neither a shift in the absolute position of the Laue spots, nor a split, we can further infer that there is no crystal rotation or polygonization (formation of subgrain structures) in the pillar crystal upon the deformation. This is an important observation considering the huge amount of strain (~35%) to which the crystal was subjected.

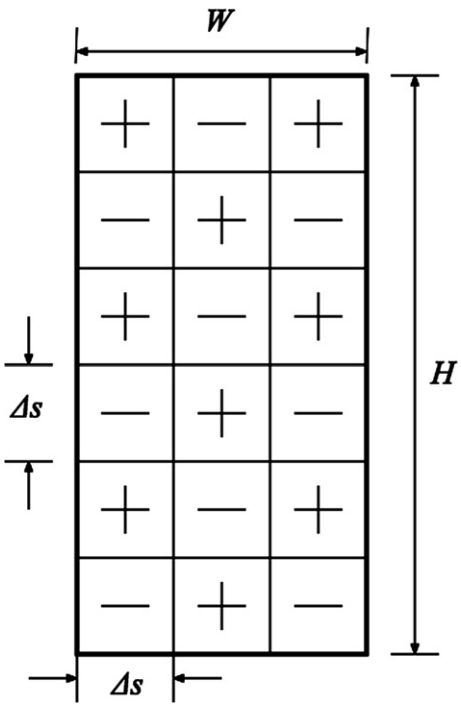

Fig. 7. A model of the pillar single-crystal consisting of different domains of size Δs, each assumed to be occupied by like-signed edge dislocations, leading to a local lattice curvature of magnitude $|\kappa|$.

This observation is consistent with the earlier TEM observations on a deformed Au pillar conducted by Greer and Nix [21]. Their TEM results showed that there were only two dislocations left in their pillar after deformation and that they were both of a non-movable type for the uniaxial compressive loading of their experiment. Both observations (the present Laue X-ray microdiffraction and the earlier TEM results) support the idea that submicron single-crystal Au pillars are nearly defect-free even after significant plastic deformation. This view was recently further supported by the in situ TEM observations of the compression of single-crystal Ni pillars by Minor et al. [31]. They found that the dislocations present in undeformed pillars (including some dislocation loops near the pillar surfaces created by FIB damage) quickly escaped from the pillar during compressive deformation, leaving the pillar free of dislocations after compression.

We may now conclude that the present white-beam X-ray microdiffraction observations, supported by the closely related TEM results [21,31], are consistent with the model of hardening of small crystals by dislocation starvation and dislocation nucleation or source-controlled plasticity, as suggested by Greer and Nix [21]. In ordinary plasticity (i.e. in typical bulk samples), dislocation motion leads to dislocation multiplication by various cross-slip processes, invariably leading to softening before strain hardening occurs through elastic interaction of dislocations. However in small samples, such as the submicron Au single-crystal pillar under study here, dislocations can travel only very small distances before annihilating at free surfaces, thereby reducing the overall dislocation multiplication rate. The central idea is that, as dislocations leave the crystal more frequently than they multiply, the crystal can quickly reach a dislocation-starved state. When such a state is reached, continued loading would force other, harder sources of dislocations to be activated in the crystal, leading to the abrupt rise in the measured flow stress (i.e. hardening).

4. Conclusions

Using synchrotron white-beam X-ray submicron diffraction, we have studied a submicron single-crystal Au pillar, before and after uniaxial plastic deformation, and found no evidence of measurable lattice rotation or lattice curvature caused by the deformation, even though a plastic strain of about 35% was imposed and a high flow stress of close to 300 MPa was achieved in the course of deformation. These observations, coupled with other examinations using electron microscopy, suggest that plasticity here is not controlled by strain gradients, but rather by dislocation source starvation, with smaller volumes being stronger because fewer sources of dislocations are available. The central idea of this model is that for very small crystals, dislocations leave the crystal more frequently than they multiply, forcing other, harder sources of dislocations to be activated. Understanding and controlling the mechanical properties of materials on this scale may thus lead to new and more robust nanomechanical structures and devices.

Acknowledgements

This work was supported by the Office of Science, Office of Basic Energy Sciences, of the US Department of Energy under Contract Nos. DE-FG02-04ER46163 and DE-AC02-05CH11231. Additional support though an NSF-EU Collaborative Research Program: NANOMESO under NSF Grant No. 0502208 is gratefully acknowledged.

References

[1] Arzt E. Acta Mater 1998;46:5611.
[2] Yu DY, Spaepen F. J Appl Phys 2003;95:2991.
[3] Nix WD. Metall Trans A 1989;20A:2217.
[4] Stelmashenko NA, Walls MG, Brown LM, Millman YV. Acta Metall Mater 1993;41:2855.
[5] De Guzman MS, Neubauer G, Flinn P, Nix WD. Mater Res Soc Proc 1993;308:613.
[6] Ma Q, Clarke DR. J Mater Res 1995;10:853.
[7] Poole WJ, Ashby MF, Fleck NA. Scripta Mater 1996;34:559.
[8] Nix WD, Gao H. J Mech Phys Solids 1998;46:411.
[9] Gao H, Huang Y. Naturwissenschaftler 1999;86:507.
[10] Gao H, Huang Y, Nix WD, Hutchinson JW. J Mech Phys Solids 1999;47:1239.
[11] Huang Y, Chen JY, Guo TF, Zhang L, Hwang KC. Int J Fract 1999;100:1.
[12] Huang Y, Gao H, Nix WD, Hutchinson JW. J Mech Phys Solids 2000;48:99.
[13] Huang Y, Xue Z, Gao H, Nix WD, Xia ZC. J Mater Res 2000;15:1786.
[14] Tymiak NI, Kramer DE, Bahr DF, Wyrobek TJ, Gerberich WW. Acta Mater 2001;49:1021.
[15] Swadener JG, George EP, Pharr GM. J Mech Phys Solids 2002;50:681.
[16] Durst K, Backes B, Goken M. Scripta Mater 2005;52:1093.
[17] Durst K, Backes B, Franke O, Goken M. Acta Mater 2006;54:2547.
[18] Basinski SJ, Basinski ZS. Plastic deformation and work hardening. In: Nabarro FRN, editor. Dislocations of Solids. Dislocations in Metallurgy, vol. 4. Oxford: North-Holland; 1979. p. 261.
[19] Uchic MD, Dimiduk DM, Florando JN, Nix WD. Science 2004;305:986.
[20] (a) Greer JR, Oliver WC, Nix WD. Acta Mater 2005;53:1821
(b) Greer JR. PhD dissertation, Stanford University; 2005.
[21] Greer JR, Nix WD. Phys Rev B 2006;73:245410.
[22] Valek BC. PhD dissertation, Stanford University; 2003.
[23] Budiman AS, Tamura N, Valek BC, Gadre K, Maiz J, Spolenak R, et al. Appl Phys Lett 2006;88:233515.
[24] Maurel A, Mercier J, Lund F. Phys Rev B 2004;70:024303.
[25] Tamura N, MacDowell AA, Spolenak R, Valek BC, Bravman JC, Brown WL, et al. J Synchrotron Rad 2003;10:137.
[26] Han SM. PhD dissertation, Stanford University; 2006.
[27] Maass R, Grolimund D, Petegem S, Willimann M, Jensen M, Swygenhoven H, et al. Appl Phys Lett 2006;89:151905.
[28] MacDowell AA, Celestre RS, Tamura N, Spolenak R, Valek BC, Brown WL, et al. Nucl Instrum Meth Phys Res A 2001;467–468:936.
[29] Cahn RW. J Inst Met 1949;86:121.
[30] Nye JF. Acta Metall 1953;1:153.
[31] Shan ZW, Mishra R, Syed Asif SA, Warren OL, Minor AM. Unpublished research; 2007.